Visible-light-active g-C3N4/N-doped Sr2Nb2O7 Heterojunctions as Photocatalysts for the Hydrogen Evolution Reaction

Journal Name

ARTICLE

Visible-light-active g-C₃N₄/N-doped Sr₂Nb₂O₇ Heterojunctions as Photocatalysts for the Hydrogen Evolution Reaction

Shiba P. Adhikari[a,b,‡], Zachary D. Hood[c,d,+], Vincent W. Chen[c], Karren L. More[d], Keerthi Senevirathne[e], and Abdou Lachgar[a,b,*]

Different visible-light-active g-C₃N₄/nitrogen-doped Sr₂Nb₂O₇ heterojunction photocatalysts were fabricated by deposition of graphitic carbon nitride over N-doped strontium pyro-niobate prepared by ammonolysis at different temperatures of solvothermally synthesized Sr₂Nb₂O₇ nanorods. Their photocatalytic performance was determined by the amount of hydrogen generated from water reduction under visible light irradiation. The best performing heterojunction was found to be the one formed by g-C₃N₄ and N-doped Sr₂Nb₂O₇ obtained at 700 °C. The enhanced activity of the heterojunction can be explained by better charge separation due to proper bands allignment, and intimate contact between the heterojunction components as revealed by electron microscopy. A mechanism for the observed enhanced photocatalytic activity is proposed and supported by band position calculations and photoluminescence data.

Keywords: g-C₃N₄, Heterojunction, Hydrogen, N-doping, Photocatalyst, Strontium niobate

1. Introduction

Semiconductor-based heterogeneous photocatalysis utilizing solar energy is a green technology that has the potential to address the environmental impacts of fossil fuels. The discovery of photo-electrochemical splitting of water using n-TiO₂ anode in the early 1970s led to the study of numerous semiconductors such as oxides, sulfides, and oxynitrides as potential photocatalysts for solar fuels generation and environmental remediation.[1–5] However, most photocatalysts studied have wide band gaps and therefore are active only under UV irradiation. To maximize the use of solar radiation, the photo-response of the catalysts should be in the visible region of the electromagnetic spectrum since visible light accounts for about half of the solar energy spectrum while UV radiation makes up approximately 4%. Therefore, developing photocatalysts with a high activity and good photochemical stability under visible light is highly desirable.[6–9]

To overcome the limitation that most oxides are only UV responsive, different methods have been developed to extend their light absorption range into visible. These include doping with metal and/or non-metal ions and surface modifications such as the formation of heterojunctions by combining the oxide with metals or other semiconductors. Cation doping creates acceptor states below the conduction band, and anion doping creates donor states above the valence band. The net result is smaller band gaps. The study of N-doped TiO₂ by Asahi and co-workers in 2001,[7] led to extensive studies on visible-light-active semiconductors doped with non-metallic elements such as nitrogen, sulfur, and carbon. Irie *et al.* described the effect of the amount of nitrogen concentration on the photocatalytic activity of TiO₂₋ₓNₓ microcrystalline powders prepared by annealing TiO₂ anatase in ammonia.[10] Anion (nitrogen and sulfur) doping was extended to oxides with layered perovskite or pyrochlore structure-types. Thus, several nitrogen-doped (N-doped) perovskites and pyrochlores including NaTaO₃, SrTiO₃, Sr₂Ta₂O₇, Ba₅Ta₄O₁₅, CsTaWO₆, Ca₂Nb₃O₁₀, CsCa₂Ta₃O₁₀ have been reported to possess wide visible light absorption.[11–18]

Semiconductor heterojunctions have emerged as an effective approach to inhibit charge carriers recombination and maximize visible light absorption.[19–22] Properly designed heterojunctions have been shown to lead to separation of photogenerated electron-hole pairs, thus increasing their lifetime so they can participate in surface redox processes. A number of heterojunctions were fabricated and their photocatalytic performances were examined in a variety of applications including water splitting, CO₂ reduction, and toxic organics degradation.[23–27]

[a] Department of Chemistry, Wake Forest University, Winston-Salem, NC 27109, USA
[b] Center for Energy, Environment and Sustainability (CEES), Wake Forest University, Winston-Salem, NC 27109
[c] School of Chemistry and Biochemistry, Georgia Institute of Technology, Atlanta, GA 30332, USA
[d] Center for Nanophase Materials Sciences, Oak Ridge National Laboratory, Oak Ridge, TN 37831, USA
[e] Department of Chemistry, Florida Agricultural and Mechanical University, Tallahassee, FL 32307, USA
‡ Current address: Materials Science and Technology Division (MSTD), Oak Ridge National Laboratory, Oak Ridge, Tennessee, 37831, USA

+ Current address: Electrochemical Materials Laboratory, Department of Materials Science and Engineering, Massachusetts Institute of Technology, Cambridge, MA 02139, USA

* lachgar@wfu.edu; Fax: +1-336-758-4656; Tel: +1-336-758-4676

In the search for robust and stable visible light active photocatalysts, graphitic carbon nitride (g-C$_3$N$_4$) with a band-gap of about 2.7 eV was studied extensively.[28,29] In comparison to metal-based photocatalysts, g-C$_3$N$_4$ can be easily prepared by thermal polycondensation of nitrogen-rich organic precursors such as cyanamide, dicyandiamide, melamine, and urea.[28,30–33] However, the photocatalytic efficiency of g-C$_3$N$_4$ is unsatisfactory due to high recombination rate of photogenerated electron-hole pairs, thus several g-C$_3$N$_4$ containing heterojunctions have been successfully fabricated and found to display significantly higher photocatalytic activity under visible light irradiation.[34–48]

Taking into account the benefits of designing and constructing heterojunction photocatalysts, we recently reported the photocatalytic activity of g-C$_3$N$_4$/Sr$_2$Nb$_2$O$_7$.[49] The incorporation of g-C$_3$N$_4$ in Sr$_2$Nb$_2$O$_7$ not only extends light absorption range of Sr$_2$Nb$_2$O$_7$ but more importantly, significantly enhances its photocatalytic activity. The rate of photocatalytic hydrogen production from water reduction under visible light was found to be 11 times larger for the g-C$_3$N$_4$/Sr$_2$Nb$_2$O$_7$ heterojunction compared to g-C$_3$N$_4$. The choice of Sr$_2$Nb$_2$O$_7$ for the construction of g-C$_3$N$_4$/Sr$_2$Nb$_2$O$_7$ heterojunction was purely based on the presence of layered structure, which has attracted wide interest owing to its high quantum yield for photocatalytic water splitting.[50,51] We have extended this work by studying the photocatalytic activity of heterojunctions based on g-C$_3$N$_4$ and N-doped Sr$_2$Nb$_2$O$_7$ synthesized by ammonolysis at different temperatures of solvothermally prepared Sr$_2$Nb$_2$O$_7$ in order to further enhance the photocatalytic performance of the semiconductor heterojunction. This study gives the comparative outlook of the effect of N-doping on photocatalytic activities of heterojunctions by taking into the account of N doped and undoped Sr$_2$Nb$_2$O$_7$ while forming the heterojunction with g-C$_3$N$_4$. Although it has been reported that the N doping of niobate based semiconductors suffers from damage due to nitridization during ammonolysis[52,53], there is not any report out there comparing the effect of N doping on Sr$_2$Nb$_2$O$_7$ and studying the photocatalytic effects by creating the heterojunction photocatalysts. The heterojunctions and their individual components were characterized by a number of analytic techniques, including PXRD, FTIR, TGA/DSC, STEM, SEM-EDS, TEM, DRS, PL, EIS, and BET surface area. Their photocatalytic performance was evaluated using photocatalytic reduction of water under visible light irradiation in the presence of methanol as a hole scavenger. The heterojunctions displayed better performance than their individual components. The heterojunction CN/SNON-700 was found to exhibit a remarkably enhanced photocatalytic activity of 128.8 mmol H$_2$/h/mole of CN, which is ~14× times larger than the amount of hydrogen generated from one mole of pristine CN. The enhancement factor associated for this N-doped heterojunction is significantly larger than that of the g-C$_3$N$_4$/Sr$_2$Nb$_2$O$_7$ heterojunction.[49] A mechanism for the observed enhanced photocatalytic activity is proposed based on the observed activity and band position calculations.

2. Experimental Section

2.1 Synthesis of strontium niobate (SNO) and N-doped strontium niobate (SNON-X; 'X' indicates the temperature used for ammonolysis)

Strontium pyroniobate (SNO) was prepared hydrothermally using niobium chloride (NbCl$_5$, Alfa Aesar, 99.9 %) and strontium nitrate (Sr(NO$_3$)$_2$, Sigma-Aldrich, 99.0 %) as reported in our previous

work.[49] In a typical reaction, a solution of NbCl$_5$ in ethanol (5 mmol (1.350 g) dissolved in 10 mL of ethanol) was added dropwise to an aqueous solution of Sr(NO$_3$)$_2$ (5 mmol (1.058 g) of Sr(NO$_3$)$_2$ dissolved in 10 mL of deionized water). An aqueous solution of NaOH (2M) was added to maintain the pH of the mixture at 10. A white precipitate formed after the mixture was stirred for 30 min at RT. The mixture was transferred to a 100 mL autoclave, sealed, and heated at 220 $^{\circ}$C for 24h (heating and cooling rate of 5 $^{\circ}$C/min). The strontium pyroniobate obtained (white powder, 600 mg in each case) was subjected to ammonolysis using dry NH$_3$ (flow rate: 200 mL/min) for 2 hours in a tube furnace at 600 $^{\circ}$C, 700 $^{\circ}$C, 800 $^{\circ}$C, and 950 $^{\circ}$C (heating and cooling rates of 10 $^{\circ}$C/min). The color of N-doped products ranged from yellow-white to brown as the ammonolysis temperature increased. The N-doped samples were labeled as SNON-X where X represents the temperature at which they were prepared (600, 700, 800, or 950 °C).

2.2 Synthesis of graphitic carbon nitride (g-C$_3$N$_4$) and heterojunctions

Graphitic carbon nitride (g-CN) was prepared by thermal decomposition of melamine at 525 °C in a muffle furnace for 4 hours at a heating rate of 5 °C min^{-1}. The g-C$_3$N$_4$/N-doped Sr$_2$Nb$_2$O$_7$ heterojunctions were prepared by mixing a suspension of g-C$_3$N$_4$ (200 mg of g-C$_3$N$_4$ sonicated in 25 mL of methanol for 1 hour) and a suspension of SNON-X (200 mg of SNON-X sonicated in 25 mL of methanol for 1 hour. The two suspensions were mixed and magnetically stirred at 50 °C. After 5 hours, the product was filtered and dried, thoroughly ground, then calcined at 400 °C for 4 hours under Argon flow (100 mL/min).

2.3 Characterization

Powder X-ray diffraction (PXRD) data were collected on a Bruker-D2 Phaser diffractometer, with Cu-Kα radiation (λ=0.15418 nm, 30 kV, and 10 mA). Scanning electron microscopy (SEM) images were collected on a Zeiss Ultra60 FE-SEM with an operating voltage at 5.0 kV. Energy-dispersive X-ray spectroscopy (EDS) with elemental mappings were completed on an Oxford Instruments X-Max^N at 10.0 kV. The microstructure and elemental mapping were performed on a scanning transmission electron microscope (STEM, Hitachi HF3300) at 300 kV. Differential scanning calorimetry (DSC) and thermogravimetric analysis (TGA) was completed using an SDT-Q600 (TA instrument, USA) from 32-800 °C under constant airflow (100 mL/min) and a heating rate of 10 °C/min. X-ray photoelectron spectroscopy (XPS) was performed using Kratos Axis Ultra DLD X-ray Photoelectron Spectrometer. The samples were analyzed as powders mounted on small pieces of indium metal. Brunauer-Emmett-Teller (BET) surface areas were determined from nitrogen adsorption isotherms at 77 K using Autosorb-iQ from Quantachrome. Diffuse reflectance UV-Vis spectra (DRS) were collected on an Ocean Optics FLAME-S-XR1-ES spectrophotometer equipped with an integrating sphere. Fourier transform infrared spectra (FTIR) were recorded on Spectrum 100 spectrometer (PerkinElmer). Photoluminescence (PL) and time-resolved fluorescence emission decay measurements were collected on a Horiba JobinYvon Fluorolog Fluorimeter (Model No. FL-1057) using a 450 W Xe lamp/monochromator combination and a pulsed LED (Model NanoLED N-330), respectively, as the excitation sources. The excitation monochromator was set at 336 nm to match the output of the pulsed LED for all samples for both emission and lifetime measurements. The powder samples were compacted into the

sample holder (Model No. 1933) which was oriented at 60° with respect to the excitation source to minimize scattering. All measurements were performed at room temperature. The emission signals were fitted using tri-exponential decay. The average lifetime (τ_{avg}) was determined by the following equation:

$$\tau_{avg} = \frac{\sum A_i \tau_i^2}{\sum A_i \tau_i} \qquad \text{(eq. 1)}$$

where A_i and τ_i are the amplitudes (or weighting factors) and lifetimes, respectively.

Electrochemical impedance spectra (EIS) were collected with a Gamry 3000 electrochemical workstation using a conventional three-electrode system consisting of a fluorine-doped tin oxide (FTO) glass as the working electrode, Ag/AgCl as the reference electrode, and a platinum wire as the counter electrode. The measurements were performed using a 5.0 mV AC voltage signal at 1 V vs Ag/AgCl between 100 kHz – 0.1 Hz in 0.5 M Na_2SO_4 solution. The FTO electrode was prepared by spin coating a slurry of photocatalyst on FTO glass (dimensions: 1 cm × 1 cm) and drying in an oven at 60 °C.

2.4 Photocatalytic tests

The photocatalytic performance was determined using a 300 W Xenon lamp (Newport Corporation) was used as the light source with a 420 nm cut-off filter to provide visible light irradiation only. All experiments were performed at 25 °C using a water-jacketed photocatalytic cell. In a typical photocatalytic reaction, 100 mg of the photocatalyst was dispersed in an aqueous solution of methanol (5 mL MeOH and 45 mL of deionized H_2O). Before illumination, the suspension was degassed with nitrogen gas for 30 min. The solution was exposed to visible light irradiation ($\lambda \geq 420$ nm) under magnetic stirring. The amount of hydrogen produced was quantified by gas chromatography (HP 6890 with TCD, argon carrier). For recyclability and stability tests, the suspension was degassed with nitrogen gas for 30 min before each cycle. In all cases, Pt co-catalyst (2.5 % by weight) was photo-deposited on the heterojunction particles using chloroplatinic acid hexahydrate ($H_2PtCl_6 \cdot 6H_2O$, Sigma-Aldrich) as the Pt source. In a typical reaction, 100 mg of catalyst and 6.63 mg of chloroplatinic acid hexahydrate were introduced into a pyrex photocatalytic cell with 50 mL of aqueous solution containing 10 mL of methanol. The suspension was irradiated with UV light for 4 hours with constant magnetic stirring. The gray colored Pt-coated samples were recovered by centrifugation and dried in vacuum at 60 °C for 4 hours before subsequent use. The Pt co-catalyst was loaded in all photocatalyst samples including the heterogeneous mixture (blend sample), which was used to check the photocatalytic enhancement as a control experiment. The apparent quantum yield (AQY) was calculated using the following equation:

$$AQY\ (\%) = \frac{\text{number of evolved } H_2 \text{ molecules} \times 2}{\text{number of incident photons}} \times 100 \quad (\text{eq. 2})$$

The average irradiation intensity (with bandpass filter at λ = 420 nm) was determined to be 0.45 W/cm^2 with the irradiation area of 4.12 cm^2. The numbers of incident photons (N) were calculated to be 2.80×10^{21} for one hour of irradiation. The turnover number (TON) and turnover frequencies (TOF) were calculated using the following equations.

$$TON = \frac{\text{number of moles of } H_2 \text{ evolved}}{\text{number of moles of CN in the photocatalyst}} \quad \text{(eq. 3)}$$

$$TOF = \frac{TON}{\text{Reaction time (hours)}} \quad \text{(eq. 4)}$$

To investigate the photocatalytic recyclability, three runs of the photocatalytic hydrogen generation were performed for 15 h. The water solution containing the heterojunction photocatalyst (CN/SNON-700) used for the hydrogen generation was degassed after each run by bubbling Argon gas through the solution.

3. Results and Discussions

3.1 Characterizations

Powder X-ray diffraction (PXRD) patterns of $Sr_2Nb_2O_7$ and N-doped $Sr_2Nb_2O_7$ (SNON) at different temperature are shown in Figure 1a. The PXRD pattern for $Sr_2Nb_2O_7$ obtained by the solvothermal route is consistent with that of layered perovskite prepared by high-temperature solid-state reactions.[50,54] The PXRD pattern of SNON at temperatures below 800 °C are similar to the parent oxide. The PXRD of SNON-950 indicates the formation of the cubic oxynitride $SrNbO_2N$,[55] as previously reported by Guo et. al.[56] Elemental analysis of different SNON-X showed that nitrogen content increases with increasing ammonolysis temperature (Table 1).
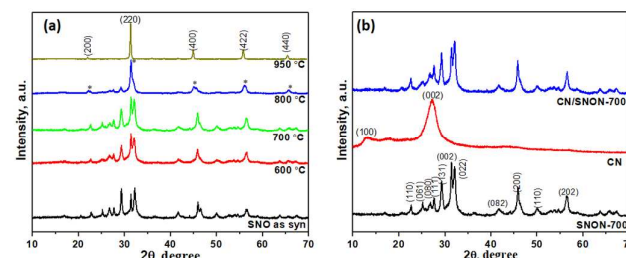

Figure 1: (a) PXRD patterns of SNO and different SNON-X. (b) The PXRD pattern of C_3N_4 and heterojunctions based on C_3N_4 and SNON-700 (∗ represents the peaks due to oxynitride phase which appears as low as 800 °C).

PXRD patterns of the SNON-700, CN and CN/SNON-700 are shown in Figure 1b. The diffraction peaks at 13.0° and 27.3° for pure CN were indexed in the hexagonal unit cell (cell parameters: a = 6.498(5) Å, c = 6.702(4) Å, and space group: $P\bar{6}$) as (100) and (002) (JCPDS 87-1526).[29,57,58] The PXRD of SNON-700 was indexed in the orthorhombic unit cell of $Sr_2Nb_2O_7$ (JCPDS 70-9937) (a=3.94269(5) Å, b=26.2057(1) Å, and c=5.6821(9) Å, and space group: $Cmc2_1$).[49] Since diffraction peaks of CN could not be clearly observed in the CN/SNON-700 heterojunction due to peak overlap, FTIR of CN/SNON-700 was collected and showed strong absorption bands in the 1200-1650 cm^{-1} region ascribed to stretching modes of CN heterocycles, and a strong band at ~804 cm^{-1} that corresponds to the characteristic stretching band of tris-triazine units, confirming the presence of CN (Figure S1, ESI).[41,59]
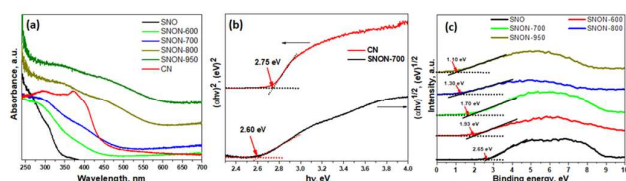
Figure 2: (a) UV-vis diffuse reflectance spectroscopy for different samples; (b) Corresponding Tauc plots for CN and SNON-700; (c) VB-XPS analysis for $Sr_2Nb_2O_7$ and all N-doped samples.

Diffuse reflectance UV-Vis spectra of all compounds studied are shown in Figure 2a. The parent oxide, $Sr_2Nb_2O_7$, possess strong absorption in UV ($\lambda \sim 350$ nm), while all SNON-X possess strong absorption in the visible ($\lambda > 420$ nm). Optical band gap energy of the semiconductors studied was determined by fitting the absorption spectra with the following equation:[60]

$$\alpha h\nu = A (h\nu - Eg)^{n/2} \qquad \text{(eq. 5)}$$

where α, h, ν, A and Eg are the absorption coefficient, Planck's constant, light frequency, proportionality constant, and band gap energy, respectively; n corresponds to the electronic transition properties of the semiconductor ($n = 1$ for a direct band-gap transition and $n = 4$ for an indirect band gap transition). The values of n for SNON-X are set at 1 assuming direct band gap transition.[56,61] Similarly, the value of n for CN is set at 4 assuming an indirect band gap system.[62–66] Using the corresponding Tauc plots (Figure 2b), the band gaps of SNON-700 and CN were calculated to be 2.60 eV and 2.75 eV, respectively.

The band gap of SNON-X (Table 1) decreases with increasing nitrogen content and temperatures and are consistent with the colors of the samples. The band positions were calculated based on band gaps, and VB positions obtained from VB-XPS data (Figure 2c). The CB positions were calculated using the following equation:

$$E_{CB} = E_{VB} - E_g \qquad \text{(eq. 6)}$$

As expected, the CB positions are virtually the same for all SNON-X, while the top of the VB is significantly affected by different N-doping resulting from ammonolysis at different temperatures (Table 1). Surface areas of SNON-X decreased with increasing sintering temperatures as shown in Table 1. Hydrothermally synthesized SNO has larger surface area than that of $Sr_2Nb_2O_7$ synthesized by solid-state reactions at high temperatures.[54,67–69] Additionally, surface areas of SNON-X were found to be larger than nitridized SNO reported by Guo et al.[56] Similar trend in surface area was observed for the heterojunctions (Table S1, ESI).

Table 1: Physical properties of different SNON-X samples.

Sample SNON-X	Band gap, eV	Band Positions based on VB XPS, eV vs NHE		Nitrogen content, wt. %	Color	Surface area, m^2/g
		VB	CB			
SNO	3.58	+2.65	-0.93	0	white	64.7
SNON-600	2.85	+1.93	-0.92	0.23	light yellow	25.1
SNON-700	2.60	+1.70	-0.90	0.73	yellow	20.3
SNON-800	2.20	+1.30	-0.90	1.72	green yellow	11.8
SNON-950	2.00	+1.10	-0.90	5.19	brown	8.2

SEM images of SNON-X (Figure S2) clearly show that the nanoplate morphology of the parent oxide (SNO) is maintained in SNON-600 and SNON-700, while larger particles were observed in SNON-800 and SNON-950 due to higher sintering temperatures. SEM images EDS mapping of different heterojunctions (Figure S3) clearly show that SNON-X were uniformly coated with g-C_3N_4.[49] High-resolution STEM images of the heterojunction made by g-C_3N_4 and SNON-700 (Figure 3) show that CN crystallizes as fibers (Figure 3a), and SNON-700 possesses nanoplate like morphology similar to the parent oxide, $Sr_2Nb_2O_7$. On the other hand, the CN/SNON-700 heterojunction sample showed that the SNON-700 nanoplates are uniformly covered by flake-like CN particles (Figure 3c). High-resolution STEM images clearly reveal the nanostructure of this particular heterojunction (Figure 3d-f), showing that intimate contact is present between its two components. SEM-EDS elemental mapping of CN/SNON-700 heterojunction (Figure 4), confirms that CN is uniformly distributed over SNON. Similarly, EDS mapping of all heterojunctions (Figure S3) clearly showed that the SNON-X samples are uniformly covered with CN particles.
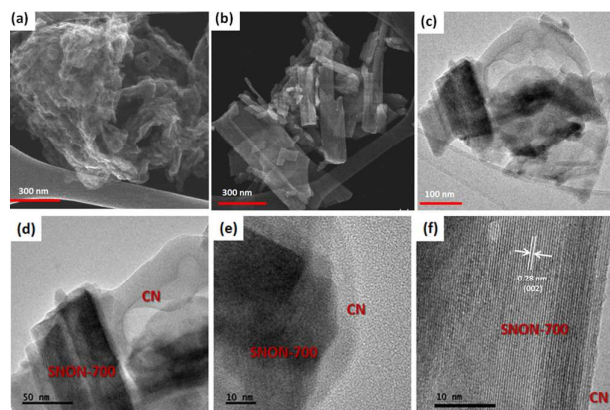

Figure 3: STEM images for (a) CN, (b) SNON-700, (c) CN/SNON-700, and (d, e, f) high-resolution STEM images for CN/SNON-700.
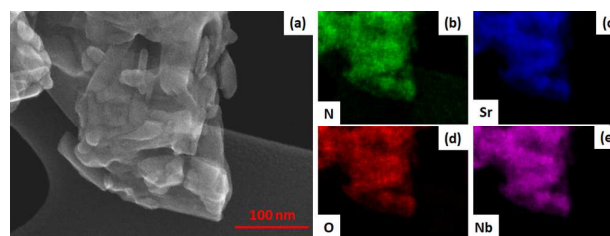

Figure 4: CN/SNON-700 heterojunction; (a) SEM and (b, c, d, and e) EDS mapping for N, Sr, O, and Nb present in the heterojunction sample, demonstrating a tight heterojunction present between the CN and SNON-700 particles.

The chemical states and compositions were further investigated using X-ray photoelectron spectroscopy (XPS). The survey XPS spectra for CN, SNON-700, and the CN/SNON-700 heterojunction

(Figure 5a) show the presence of C, N, Sr, Nb, and O in CN/SNON-700. The binding energy values for the elements in CN, SNON-700, and CN/SNON-700 heterojunction are reported in Table 2. The high-resolution XPS spectrum of C1s (Figure 5b) in CN displays two major peaks around 284.3 and 288.1 eV, which can be attributed to sp^2 hybridized carbon from aromatic rings and sp^2 hybridized carbon in the N-C=N group, respectively.[26,41,62,70,71] Similarly, three N1s peaks (at 398.4 eV, 400.8 eV, and 404.2 eV) are observed for CN (Figure 5c). The small peak observed around 395.6 eV in the XPS spectrum of SNON-700 is assigned to N1s, confirming the N-doping. The C1s and N1s peaks in CN/SNON-700 heterojunction are found at lower binding energies than that of CN, confirming CN hybridization with SNON-700 upon heterojunction fabrication.[26,41,72,73] A similar conclusion can be made by comparing the corresponding binding energy values of Sr3d, Nb3d and O1s in SNON-700 and CN/SNON-700 heterojunction samples (Table 2 and Figure 5d-f). Furthermore, as shown in Table 2 and Figure S4 (ESI), the binding energy values for C1s, N1s, Sr3d, Nb3d and O1s in blend sample (heterogeneous mixture) are the same as those for individual components (CN and SNON-700). This result further supports the fact that CN and SNON-700 in the heterojunction are hybridized as observed in electron microscopy studies and other characterizations tools used in this study.
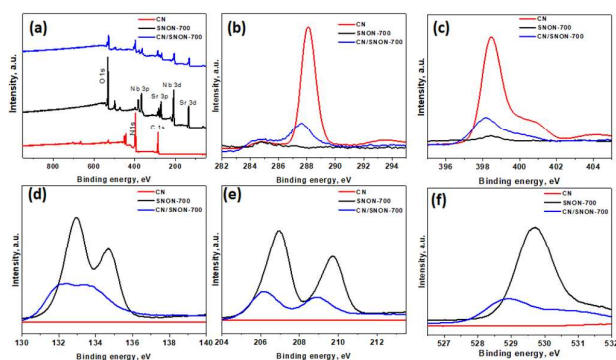

Figure 5: (a) XPS for CN, SNON-700, and CN/SNON-700. High resolution XPS spectra of (b) C 1s, (c) N1s, (d)Sr3d, (e) Nb3d, and (f) O1s for CN, SNON-700 and CN/SNON-700.

Table 2: Binding energy values for C1s, N1s, Sr3d, Nb3d and O1s in CN, SNON-700, CN/SNON-700, blend samples.

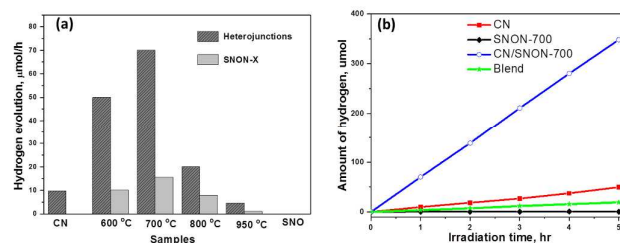| Sample	Binding Energy Values, eV				
	C1s	N1s	Sr3d	Nb3d	O1s
CN	284.6 288.1	398.4 400.8 404.0	---	---	---
SNON-700	---	398.5	132.9 134.6	206.9 209.7	529.7
CN/SNON-700	284.3 287.7	398.2 400.6 ---	132.3 133.8	206.1 208.9	528.9
Blend sample of CN and SNON-700	284.7 288.1	398.4 400.7 404.1	132.9 134.7	206.9 209.7	529.7

Figure 6: (a) Visible light-induced hydrogen evolution rates for different photocatalysts. (b) Amounts of hydrogen generated in the presence of CN, SNON-700, CN/SNON-700 heterojunction, and blend samples. Conditions: 100 mg catalyst, 50 mL 10 vol% methanol aqueous solution, 300 W Xe lamp with filter for visible light irradiation ($\lambda \geq 420$ nm).

3.2 Photocatalytic performance

The photocatalytic hydrogen production was examined under visible light irradiation ($\lambda \geq 420$ nm) in the presence of CH_3OH (10 vol. %) as a hole scavenger and 2.5 wt.% of Pt co-catalyst. SNON-X exhibited lower activities in comparison with their corresponding heterojunctions. Pure SNO does not show any activity under visible light due to its large band gap. Hydrogen evolution rates are rather low for SNON-X. This result could be attributed to high recombination rate of photo-generated charge carriers. The decreased activities observed for SNON-800 and SNON-950 could be due to the introduction of trapped states generated during harsh nitridation conditions [74,75] H_2 evolution rate for pristine CN is also low, consistent with literature values.[27,28,33,49] In contrast, all heterojunctions show higher photocatalytic activity than their individual components. The CN/SNON-700 heterojunction exhibited the best photocatalytic activity, with hydrogen evolution rate of 70 µmol/h, significantly higher than that of its individual components SNON-700 1(5.6 µmol/h) and CN (9.8 µmol/h). H_2 evolution rate observed for a blend sample, prepared by mechanically grinding CN and SNON-700, was found to be 3.6 µmol/h, which is similar to that of the pristine CN. Thus, the visible-light-induced hydrogen evolution rate for CN/SNON-700 heterojunction (128.8 mmol/h/mole of CN) is ~14× times larger than that of one mole of pristine CN slightly larger than that of our previous report on g-C_3N_4/$Sr_2Nb_2O_7$.[49] This result may be due to the involvement of both components in the absorption and charge separation.

The apparent quantum yields (AQY) were calculated to be 0.38% for CN and 3% for the CN/SNON-700 heterojunction based on the observed activity of 100 mg of the sample for 1-hour visible light irradiation ($\lambda = 420$ nm). The turnover number (TON) for CN/SNON-700 reached ~1.9 after 15 hours with a turnover frequency (TOF) of 0.12. TON and TOF were determined using the amount of hydrogen generated after 15 hours of visible light irradiation which was found to be 1033.8 µmol by 100 mg of CN/SNON-700.

Three consecutive photocatalytic water reduction experiments using the same CN/SNON-700 heterojunction sample were performed in the course of 15 hours to study its photocatalytic recyclability and stability. Aqueous suspensions containing the photocatalyst were degassed after each run by bubbling argon gas through the suspension. The total amount of hydrogen produced in the third 5-hour cycle was found to be 340 µmol, which is similar to the amount produced in the first 5-hours, 348.2 µmol. Hence, the rate of photocatalytic hydrogen production of the CN/SNON-700 sample was virtually unchanged after three cycles over a period of

15 hours (Figure S5a, ESI), indicating that the heterojunction is stable under visible light irradiation. PXRD patterns of CN/SNON-700 before and after photocatalytic reactions are also similar (Figure S5b, ESI), indicating the photochemical stability of the heterojunction under visible light irradiation.

3.3 Proposed mechanism

The improved activity of the CN/SNON heterojunction over C_3N_4 could be due to a more efficient charge separation of photogenerated electron-hole pairs. To elucidate the mechanism of the enhanced photocatalytic activity of the CN/SNON heterojunction, the relative band positions of the two semiconductors components were considered since the band-edge potential levels play a crucial role in determining the migration pathway for the photogenerated charge carriers. The band positions were determined using VB-XPS and diffuse reflectance spectroscopy and are summarized in Table 1. The CB and VB positions for SNON-700 are found to be -0.90 eV and +1.70 eV respectively, and the CB and VB potentials for CN were determined to be -1.10 and +1.65 eV, respectively (Table 1).[49] Thus, the CB and VB of CN are higher than that of SNON-700. Under visible light irradiation, both CN and SNON-700 generate electron-hole pairs. The photogenerated electrons in the CB of CN can be transferred to the CB of SNON-700, and then injected in the Pt co-catalyst to generate hydrogen through water reduction (Figure 7). Simultaneously, the photogenerated holes in the VB of SNON-700 can be transferred to the VB of CN and then used to oxidize hole scavengers such as methanol. Thus, the better charge separation leads to a reduction of the recombination rate and results in a remarkable enhancement in the photocatalytic activity observed for the CN/SNON-700 heterojunction. To understand the effect of N-doping on visible-light-driven water splitting, we have compared the above-mentioned mechanism with the mechanism that we proposed for CN/SNO (Figure S6, ESI). Because of the different band gaps for SNO and SNON, only one component is active in visible light for CN/SNO heterojunction while both components are active in CN/SNON-700 heterojunction sample.[49,76] Hence, the mechanism for enhanced activity is totally different. In the case of CN/SNO, only CN is responsible for the generation of photogenerated electron and holes while both CN and SNON-700 are responsible in CN/SNON heterojunction, further explaining the observed enhancement in photocatalytic activity.
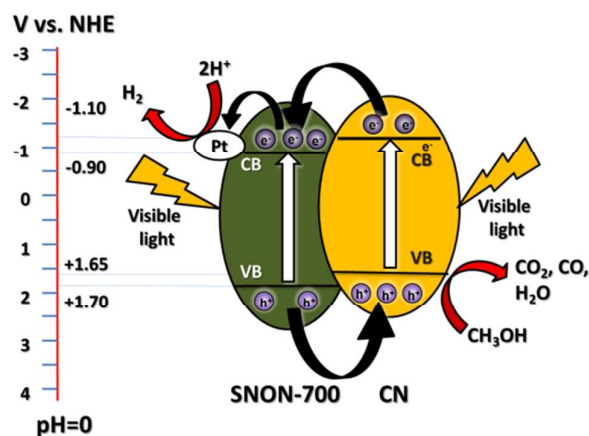

Figure 7: Schematic diagram of the mechanism of separation and transfer of photogenerated carriers in the CN/SNON-700 heterojunction under visible light irradiation.

To confirm the above-mentioned mechanism, the lifetime of photogenerated charge carriers was studied by photoluminescence (PL) experiments. The intensity of the PL emission peak centered at ~ 460 nm (Figure 8a) is in the order CN > CN/SNON-950 > CN/SNON-800 > CN/SNON-600 > CN/SNON-700.[76] In comparison to the heterojunctions, the SNON-700 sample gave no significant PL emission under the same experimental conditions (See Figure S7, ESI). This result suggests that the heterojunction made with CN and SNON-700 has lower recombination rate, consistent with the observed higher photocatalytic activity. The observed peak shape and a small blue shift in the PL emission spectrum can be explained based on nanostructured deposition of CN on SNON surfaces during heterojunction synthesis. It has been already reported that emission peak for CN in the bulk form, occurs at wavelengths between 460 to 475 nm; however, the PL peaks nay shift up to 450 nm in CN with nanosheet.[48,49,75] So, in the case of SN/SNON-700 and other heterojunctions, CN may have been deposited in the form of nanosheet. This is supported by the STEM images as shown in Figure 3.

To determine the lifetime of photogenerated electron-hole pairs, time-resolved fluorescence emission spectra were collected for CN and all heterojunctions samples (Figure 8b). The fluorescence intensities were best fitted using a tri-exponential curve.[32,77,78] The kinetic parameters for the materials studied are summarized in Table S2, ESI, where three radiative lifetimes and their relative amplitudes are reported.
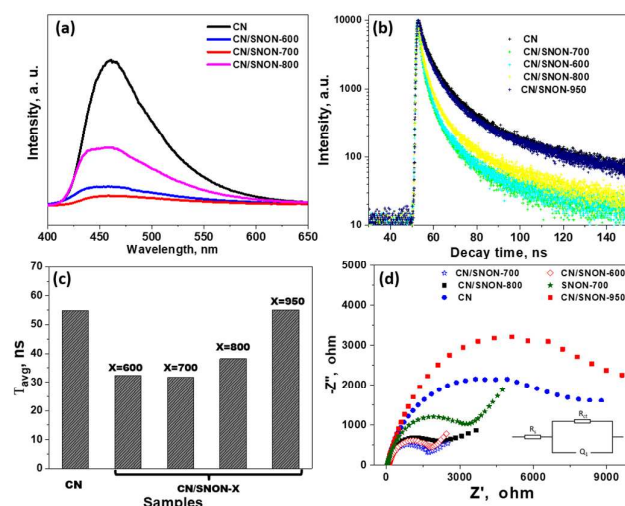

Figure 8: (a) Photoluminescence (PL) spectra of CN and CN/SNON-X at an excitation wavelength of 336 nm; (b) Time-resolved fluorescence emission decay curves for g-C_3N_4 and CN/SNON-X. The emission wavelength was set at 460 nm, with the excitation wavelength at 336 nm; (c) Weighted average lifetimes (τ_{avg}) for g-C_3N_4 and heterojunctions CN/SNON-X; (d) Electrochemical impedance spectra (EIS) of photocatalysts studied.

The weighted average lifetimes (τ_{avg}) show that the radiative lifetime of the charge carriers is higher for CN (54.8 ns). The average lifetimes for CN/SNON-700 (31.6 ns) and CN/SNON-600 (32.4 ns) are lower than that of other heterojunctions. The lower lifetime of electrons suggests that photo-generated electrons in the conduction band of CN undergo rapid transfer to CB of SNON-700 or SNON-600, which result in a better separation of charge carriers. The fast electron injection confirms that the formation of the heterojunction promotes charge transfer efficiency, which enhances the photocatalytic generation of hydrogen.[79,80] The PL data (Figure 8, a, b, c) show that CN/SNON-800 and SN/SNON-950 heterojunctions exhibit more charge recombination than CN/SNON-600 and CN/SNON-700. This property may be explained by the introduction of new trapped states during the N-doping for these high-temperature nitridized samples (800 and 950 °C).

Electrochemical impedance spectra (EIS) showed better charge transfer between the photocatalysts and the electrolyte. The high-frequency region denotes charge-transfer resistance at the CN/SNON-700/FTO interfaces, while the low-frequency region is associated with the electron transport kinetics at the CN/SNON-700 interface. The Nyquist plots can be interpreted based on the equivalent circuits, as shown as an inset in Figure 8d. A smaller arc radius in EIS Nyquist plots indicates a higher reaction rate.[72,81–83] The arc radius for the CN/SNON-700 heterojunction was found to be significantly smaller than that of its components CN and SNON-700, suggesting lower resistance to charge transfer at the interface between the electrode and electrolyte. The observed decrease of impedance in EIS suggests that photogenerated electrons have a higher probability to participate in redox reactions at the surface of photocatalysts obatained at temperatures between 600-800 °C (especially for CN/SNON-700). The reduction in the charge-transfer resistance further supports experimental evidence that CN/SNON-700 has a higher photocatalytic hydrogen evolution compared compared to pristine CN and SNON.

4. Conclusions

In summary, CN/SNON-X heterojunctions were fabricated and found to be photocatalytically active under visible light irradiation. The heterojunctions were found to exhibit higher photocatalytic efficiency than their individual components. The optimum activity was found for the CN/SNON-700, where the rate of photocatalytic hydrogen production under visible light was found to be ~14× larger than that of pristine CN. The mechanism of the charge carriers pathways at the interface between CN and SNON-700 was proposed and experimentally confirmed. The observed higher photocatalytic activity of the CN/SNON-700 heterojunction is due to suitable band positions, which allows for better charge separation.

Conflicts of interest

There are no conflicts to declare.

Acknowledgments

Notes and references

1 A. Fujishima and K. Honda, *Nature*, 1972, **238**, 37–38.
2 M. Ahmed and G. Xinxin, *Inorg. Chem. Front.*, 2016, **3**, 578–590.
3 W. Jiao, L. Wang, G. Liu, G. Q. (Max) Lu and H.-M. Cheng, *ACS Catal.*, 2012, **2**, 1854–1859.
4 A. Kumar, A. S. Patel and T. Mohanty, *J. Phys. Chem. C*, 2012, **116**, 20404–20408.
5 A. Mills and S. Le Hunte, *Journal of Photochemistry & Photobiology, A: Chemistry*, 1997, **108**, 1–35.
6 M. Ni, M. K. H. Leung, D. Y. C. Leung and K. Sumathy, *Renewable and Sustainable Energy Reviews*, 2007, **11**, 401–425.
7 R. Asahi, T. Morikawa, T. Ohwaki, K. Aoki and Y. Taga, *Science*, 2001, **293**, 269–271.
8 P. Kanhere and Z. Chen, *Molecules*, 2014, **19**, 19995–20022.
9 C.-H. Liao, C.-W. Huang and J. C. S. Wu, *Catalysts*, 2012, **2**, 490–516.
10 H. Irie, Y. Watanabe and K. Hashimoto, *J. Phys. Chem. B*, 2003, **107**, 5483–5486.
11 Y. Matsumoto, M. Koinuma, Y. Iwanaga, T. Sato and S. Ida, *J. Am. Chem. Soc.*, 2009, **131**, 6644–6645.
12 A. Mukherji, R. Marschall, A. Tanksale, C. Sun, S. C. Smith, G. Q. Lu and L. Wang, *Advanced Functional Materials*, 2011, **21**, 126–132.
13 A. Mukherji, B. Seger, G. Q. (Max) Lu and L. Wang, *ACS Nano*, 2011, **5**, 3483–3492.
14 A. Mukherji, C. Sun, S. C. Smith, G. Q. Lu and L. Wang, *J. Phys. Chem. C*, 2011, **115**, 15674–15678.
15 X. Wang, G. Liu, Z.-G. Chen, F. Li, G. Q. Lu and H.-M. Cheng, *Chemistry Letters*, 2009, **38**, 214–215.
16 J. Xu, Y. Wei, Y. Huang, J. Wang, X. Zheng, Z. Sun, L. Fan and J. Wu, *Ceramics International*, 2014, **40**, 10583–10591.
17 X. Zong, C. Sun, Z. Chen, A. Mukherji, H. Wu, J. Zou, S. C. Smith, G. Q. Lu and L. Wang, *Chem. Commun.*, 2011, **47**, 6293–6295.
18 F. Zou, Z. Jiang, X. Qin, Y. Zhao, L. Jiang, J. Zhi, T. Xiao and P. P. Edwards, *Chem. Commun.*, 2012, **48**, 8514–8516.
19 R. Marschall, *Advanced Functional Materials*, 2014, **24**, 2421–2440.
20 H. Wang, L. Zhang, Z. Chen, J. Hu, S. Li, Z. Wang, J. Liu and X. Wang, *Chem. Soc. Rev.*, 2014, **43**, 5234–5244.
21 S. J. A. Moniz, S. A. Shevlin, D. J. Martin, Z.-X. Guo and J. Tang, *Energy Environ. Sci.*, 2015, **8**, 731–759.
22 Pankaj Chowdhury, Hassan Gomaa and Ajay K. Ray, in *Sustainable Nanotechnology and the Environment: Advances and Achievements*, American Chemical Society, 2013, vol. 1124, pp. 231–266.
23 S. P. Adhikari, H. Dean, Z. D. Hood, R. Peng, K. L. More, I. Ivanov, Z. Wu and A. Lachgar, *RSC Adv.*, 2015, **5**, 91094–91102.
24 S. P. Adhikari, Z. D. Hood, K. L. More, I. Ivanov, L. Zhang, M. Gross and A. Lachgar, *RSC Adv.*, 2015, **5**, 54998–55005.
25 S. P. Adhikari, L. Zhang, M. Gross and A. Lachgar, *MRS Online Proceedings Library*, 2015, **1738**, null-null.

26 H. Shi, G. Chen, C. Zhang and Z. Zou, *ACS Catal.*, 2014, **4**, 3637–3643.

27 S. P. Adhikari, Z. D. Hood, H. Wang, R. Peng, A. Krall, H. Li, V. W. Chen, K. L. More, Z. Wu, S. Geyer and A. Lachgar, *Applied Catalysis B: Environmental*, 2017, **217**, 448–458.

28 S. Cao and J. Yu, *J. Phys. Chem. Lett.*, 2014, **5**, 2101–2107.

29 X. Wang, K. Maeda, A. Thomas, K. Takanabe, G. Xin, J. M. Carlsson, K. Domen and M. Antonietti, *Nat Mater*, 2009, **8**, 76–80.

30 D. J. Martin, K. Qiu, S. A. Shevlin, A. D. Handoko, X. Chen, Z. Guo and J. Tang, *Angewandte Chemie*, 2014, **126**, 9394–9399.

31 S. C. Yan, Z. S. Li and Z. G. Zou, *Langmuir*, 2009, **25**, 10397–10401.

32 Y. Zhang, Q. Pan, G. Chai, M. Liang, G. Dong, Q. Zhang and J. Qiu, *Scientific Reports*, 2013, **3**, 1943.

33 S. Martha, A. Nashim and K. M. Parida, *J. Mater. Chem. A*, 2013, **1**, 7816–7824.

34 S.-W. Cao, X.-F. Liu, Y.-P. Yuan, Z.-Y. Zhang, Y.-S. Liao, J. Fang, S. C. J. Loo, T. C. Sum and C. Xue, *Applied Catalysis B: Environmental*, 2014, **147**, 940–946.

35 L.-Y. Chen and W.-D. Zhang, *Applied Surface Science*, 2014, **301**, 428–435.

36 S. Chengjie, F. Mingshan, H. Bo, C. Tianjun, W. Liping and S. Weidong, *CrystEngComm*, 2015, **17**, 4575–4583.

37 Y. Cui, *Chinese Journal of Catalysis*, 2015, **36**, 372–379.

38 F. Dong, Z. Zhao, T. Xiong, Z. Ni, W. Zhang, Y. Sun and W.-K. Ho, *ACS Applied Materials & Interfaces*, 2013, **5**, 11392–11401.

39 J. Fu, B. Chang, Y. Tian, F. Xi and X. Dong, *J. Mater. Chem. A*, 2013, **1**, 3083–3090.

40 L. Ge, C. Han and J. Liu, *Applied Catalysis B: Environmental*, 2011, **108**–**109**, 100–107.

41 C. Han, Y. Wang, Y. Lei, B. Wang, N. Wu, Q. Shi and Q. Li, *Nano Research*, 2015, **8**, 1199–1209.

42 H. W. Kang, S. N. Lim, D. Song and S. B. Park, *International Journal of Hydrogen Energy*, 2012, **37**, 11602–11610.

43 W. Liu, M. Wang, C. Xu and S. Chen, *Chemical Engineering Journal*, 2012, **209**, 386–393.

44 C. Miranda, H. Mansilla, J. Yáñez, S. Obregón and G. Colón, *Journal of Photochemistry and Photobiology A: Chemistry*, 2013, **253**, 16–21.

45 C. Pan, J. Xu, Y. Wang, D. Li and Y. Zhu, *Advanced Functional Materials*, 2012, **22**, 1518–1524.

46 J.-X. Sun, Y.-P. Yuan, L.-G. Qiu, X. Jiang, A.-J. Xie, Y.-H. Shen and J.-F. Zhu, *Dalton Trans.*, 2012, **41**, 6756–6763.

47 X. Wang, L. Zhang, H. Lin, Q. Nong, Y. Wu, T. Wu and Y. He, *RSC Adv.*, 2014, **4**, 40029–40035.

48 Z. Zhang, K. Liu, Z. Feng, Y. Bao and B. Dong, *Scientific Reports*, 2016, **6**, 19221.

49 S. P. Adhikari, Z. D. Hood, K. L. More, V. W. Chen and A. Lachgar, *ChemSusChem*, 2016, **9**, 1869–1879.

50 A. Kudo, H. Kato and S. Nakagawa, *J. Phys. Chem. B*, 2000, **104**, 571–575.

51 L. Botao, M. Junfeng, Y. Yan, L. Jun, R. Yang, J. Xiaohui, S. Yong and L. Zhensen, *Journal of the American Ceramic Society*, **91**, 1329–1331.

52 M. Kodera, M. Katayama, T. Hisatomi, T. Minegishi and K. Domen, *CrystEngComm*, 2016, **18**, 3186–3190.

53 H. Suzuki, O. Tomita, M. Higashi, A. Nakada and R. Abe, *Applied Catalysis B: Environmental*, 2018, **232**, 49–54.

54 S. M. Ji, P. H. Borse, H. G. Kim, D. W. Hwang, J. S. Jang, S. W. Bae and J. S. Lee, *Phys Chem Chem Phys*, 2005, **7**, 1315–1321.

55 K. Maeda, M. Higashi, B. Siritanaratkul, R. Abe and K. Domen, *J. Am. Chem. Soc.*, 2011, **133**, 12334–12337.

56 J. Guo, H. Zhou, S. Ouyang, T. Kako and J. Ye, *Nanoscale*, 2014, **6**, 7303–7311.

57 Y. Wang, X. Wang and M. Antonietti, *Angewandte Chemie International Edition*, 2012, **51**, 68–89.

58 H. Yan, *Chem. Commun.*, 2012, **48**, 3430–3432.

59 J. Yu, S. Wang, J. Low and W. Xiao, *Phys. Chem. Chem. Phys.*, 2013, **15**, 16883–16890.

60 A. B. Murphy, *Solar Energy Materials and Solar Cells*, 2007, **91**, 1326–1337.

61 V. V. Atuchin, J.-C. Grivel, A. S. Korotkov and Z. Zhang, *Journal of Solid State Chemistry*, 2008, **181**, 1285–1291.

62 M. Tahir, C. Cao, N. Mahmood, F. K. Butt, A. Mahmood, F. Idrees, S. Hussain, M. Tanveer, Z. Ali and I. Aslam, *ACS Appl. Mater. Interfaces*, 2014, **6**, 1258–1265.

63 K. Shimizu, Y. Tsuji, T. Hatamachi, K. Toda, T. Kodama, M. Sato and Y. Kitayama, *Phys. Chem. Chem. Phys.*, 2004, **6**, 1064–1069.

64 K. Shimizu, Y. Tsuji, M. Kawakami, K. Toda, T. Kodama, M. Sato and Y. Kitayama, *Chemistry Letters*, 2002, **31**, 1158–1159.

65 S. Liang, L. Shen, J. Zhu, Y. Zhang, X. Wang, Z. Li, L. Wu and X. Fu, *RSC Adv.*, 2011, **1**, 458–467.

66 X. Xin, J. Lang, T. Wang, Y. Su, Y. Zhao and X. Wang, *Applied Catalysis B: Environmental*, 2016, **181**, 197–209.

67 B. Brahmaroutu, G. L. Messing and S. Trolier-McKinstry, *Journal of the American Ceramic Society*, 1999, **82**, 1565–1568.

68 N. Ishizawa, F. Marumo, T. Kawamura and M. Kimura, *Acta Crystallographica Section B*, 1975, **31**, 1912–1915.

69 S. Khademinia and M. Behzad, *Advanced Powder Technology*, 2015, **26**, 644–649.

70 Y. Cui, Z. Ding, X. Fu and X. Wang, *Angewandte Chemie International Edition*, 2012, **51**, 11814–11818.

71 S. Wang, C. Li, T. Wang, P. Zhang, A. Li and J. Gong, *J. Mater. Chem. A*, 2014, **2**, 2885–2890.

72 L. Huang, L. Xu, Y. Li, H. Li, X. Cheng, J. Xia, Y. Xu and G. Cai, *Dalton Trans.*, 2013, **42**, 8606–8616.

73 T. Yan, Q. Yan, X. Wang, H. Liu, M. Li, S. Lu, W. Xu and M. Sun, *Dalton Trans.*, 2015, **44**, 1601–1611.

74 T. Takata, C. Pan and K. Domen, *ChemElectroChem*, **3**, 31–37.

75 T. Takata, C. Pan and K. Domen, *Science and Technology of Advanced Materials*, 2015, **16**, 033506.

76 S. P. Adhikari, Z. D. Hood and A. Lachgar, *MRS Advances*, 2018, 1–8.

77 P. Niu, L. Zhang, G. Liu and H.-M. Cheng, *Advanced Functional Materials*, 2012, **22**, 4763–4770.

78 S. Nayak, L. Mohapatra and K. Parida, *J. Mater. Chem. A*, 2015, **3**, 18622–18635.

79 Z. Sun, H. Zheng, J. Li and P. Du, *Energy Environ. Sci.*, 2015, **8**, 2668–2676.

80 S.-W. Cao, X.-F. Liu, Y.-P. Yuan, Z.-Y. Zhang, Y.-S. Liao, J. Fang, S. C. J. Loo, T. C. Sum and C. Xue, *Applied Catalysis B: Environmental*, 2014, **147**, 940–946.

81 H. Huang, L. Liu, Y. Zhang and N. Tian, *RSC Adv.*, 2015, **5**, 1161–1167.

82 Z. Hosseini, N. Taghavinia, N. Sharifi, M. Chavoshi and M. Rahman, *J. Phys. Chem. C*, 2008, **112**, 18686–18689.

83 X. Bai, L. Wang and Y. Zhu, *ACS Catalysis*, 2012, **2**, 2769–2778.

TOC Entry
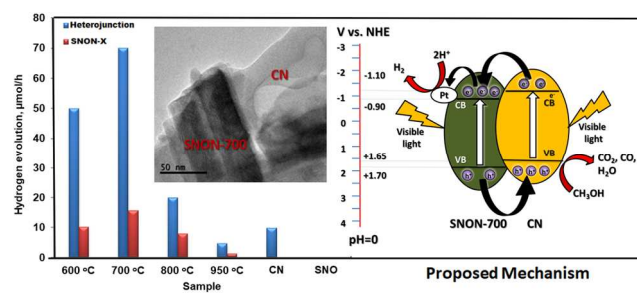
Visible light active photocatalytic performance of g-C$_3$N$_4$/NSON-X heterojunctions